communications materials

A Nature Portfolio journal

Article

https://doi.org/10.1038/s43246-026-01420-6

Uncovering the thermolysis conversion mechanisms of 3D nanoprinted silica glass

Check for updates

Jiajie Liang[1], Lisa Hoffmann[1,2], Paul Albrecht[1,2] & Jens Bauer[1,2] ✉

Thermal conversion post-processing routes expand two-photon polymerization (2PP) 3D printing from polymers to inorganics, enabling free-form micro- and nanostructures from a growing bandwidth of glasses, ceramics and metals. Yet, limited knowledge on precise transformation mechanisms remains a key obstacle to advancing the approach towards widespread applicability. This paper establishes a fundamental understanding of the thermal conversion manufacturing of silica glass from hybrid organic-inorganic preforms, 2PP-printed from a polyhedral oligomeric silsesquioxane (POSS) feedstock resist. We present correlated thermal, mechanical, and spectroscopic analyses, which resolve key microstructural transformations and resulting dimensional, chromatic and mechanical mechanisms. The thermolysis accesses a wide range of mechanical properties from compliant rubber-like to ceramic-hard with an ultra-high tensile strength of 6 GPa. The introduced correlative methodology and obtained understanding are expected to translate across different routes, providing fundamental groundwork for the rational design of advanced thermal conversion protocols for the precision manufacturing of 3D high-fidelity structures.

Thermal conversion routes are rapidly expanding two-photon-polymerization (2PP) 3D printing to a wide range of previously inaccessible inorganic materials[1–14]. 2PP is a leading manufacturing technique for the 3D printing of polymers at the smallest scale[15]. By scanning a focused laser spot along programmed trajectories, the technique locally solidifies photosensitive organic resists with speeds up to hundreds of millimeters per second, rapidly printing free-form micro- and nanostructures with resolutions down to a few hundred nanometers[16]. Specialized hybrid resists, which are engineered to incorporate inorganic elements, extend the approach to the printing of organic-inorganic hybrid structures. Post-print thermal treatments enable the conversion of these hybrid templates into purely inorganic components. To extract the targeted inorganics, the thermolysis processes apply inert or reducing atmospheres to thermally decompose and remove the organic constituents accompanied by a corresponding dimensional contraction. Along these lines, the manufacturing of a growing range of glasses[2–5,13,14], ceramics[6–10] and certain metals[11,12] has been demonstrated, with promising application potentials in microsystem technology and materials science[17–20].

However, despite the extensive research on thermolysis routes in 2PP-printing, the underlying conversion mechanisms remain insufficiently understood. Impurities, material porosity and in particular limited structure quality are common obstacles towards widespread applicability. Most reported processes apply empirical thermal treatments where little is known about the governing material microstructure transformation processes, as well as the corresponding mechanical property transitions that are decisive to preserving structural integrity and reproducible geometric precision.

The fabrication of high-quality fused silica glass micro- and nanostructures, via the air thermolysis of 2PP-printed templates from pre-glass resists based on polyhedral oligomeric silsesquioxane (POSS) chemistry[2] has recently received broad attention for applications in micro-optics and beyond[2,14,21,22]. Hybrid organic-inorganic POSS molecules[23] comprise an inorganic cage-shaped silicon-oxygen core, providing the source for the targeted SiO_2. To the corners of the inorganic POSS cages, cross-linkable acrylic functional groups can attach. Copolymerization of these acrylic ligands with an additional trifunctional acrylate enables efficient 2PP printing with resolution and structure quality on par with commercial purely organic resists. As-printed hybrid templates comprise a continuous molecular network where the inorganic silicon-oxygen nanoclusters are densely packed in a cross-linked organic matrix[2]. Post-print thermal treatment in air atmosphere drives off the organics. Accompanied by an isotropic linear contraction of ~40%, the POSS cages reorganize to a continuous inorganic network along thus far unknown paths. Pure silica glass is

[1]Institute of Nanotechnology (INT), Karlsruhe Institute of Technology (KIT), Karlsruhe, Germany. [2]Institute for Applied Materials (IAM), Karlsruhe Institute of Technology (KIT), Karlsruhe, Germany. ✉e-mail: jens.bauer@kit.edu

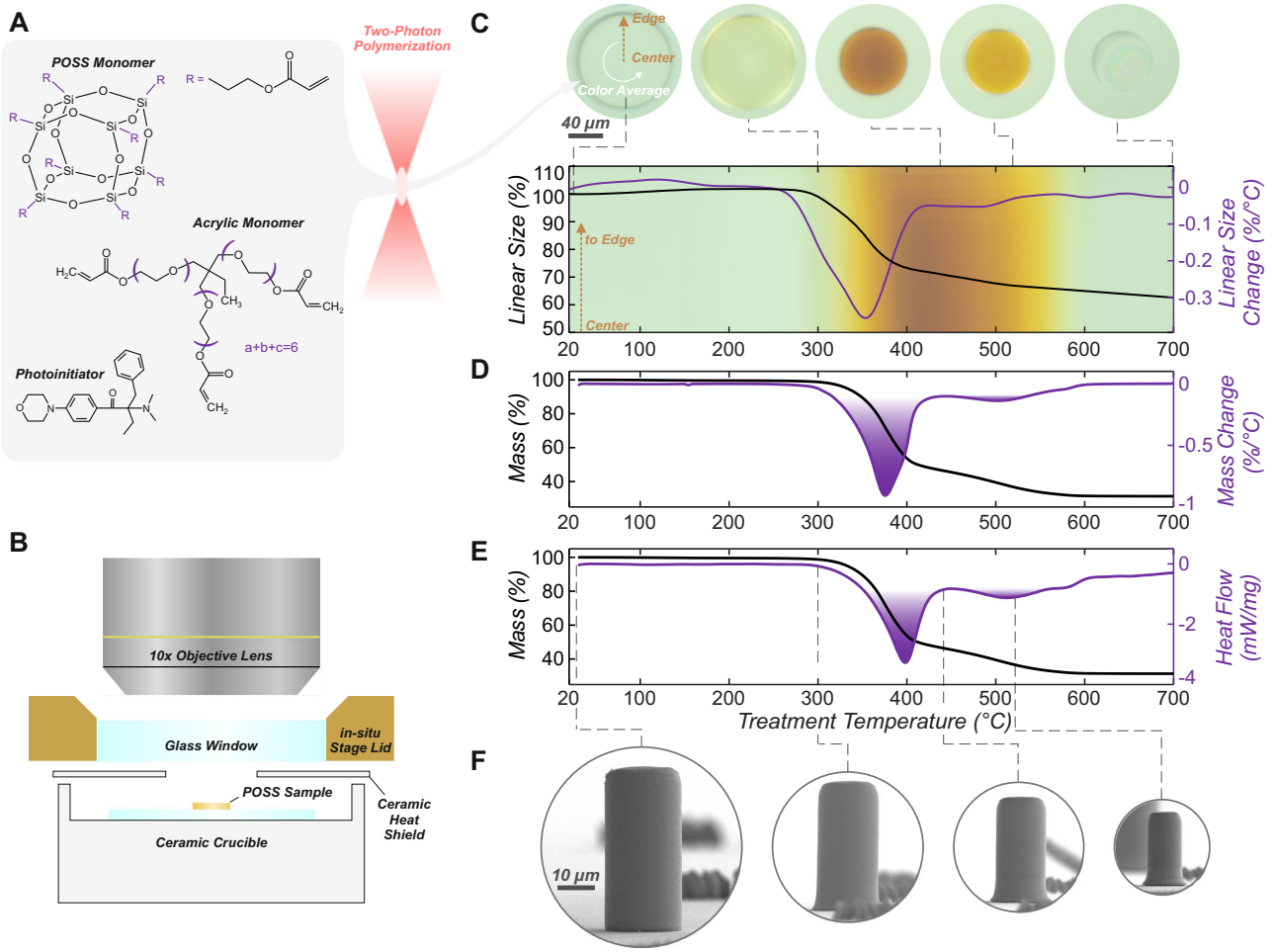


Fig. 1 | Thermal analyses of the polymer-to-glass conversion of the POSS material. A Composition of the POSS-glass resist used for specimen manufacturing. **B**, **C** Schematic in-situ micro-optical thermolysis setup and obtained size and color evolution with still frames at selected temperatures. In the color map, the vertical axis corresponds to the radial gradient from the center to the edge of the cylindrical sample. **D**, **E** Simultaneous thermogravimetric analysis (TGA) and differential scanning calorimetry (DSC) data. **F** SEM images of micropillars for mechanical testing thermolyzed at the indicated target temperatures.

formed above only 650 °C, a fraction of the sintering temperatures required to condense monolithic silica particles[13,24].

This paper establishes an in-depth understanding of the conversion mechanisms governing the thermolysis of 2PP-printed hybrid organic-inorganic materials on the microscale. Adopting the POSS-glass route as a model system, we present in-situ thermolysis analyses, micro-mechanical experiments, and optical photothermal infrared (O-PTIR) spectroscopy measurements, uncovering the interdependent dimensional, chromatic, mechanical and chemical evolution of the material's glass conversion. In particular, the process is found to proceed across three major mechanical transformations which include: the transition of the dominant load-bearer from the decomposing rubber-elastic organic matrix to the emerging inorganic silica phase, with a corresponding pronounced shift to glass-ceramic behavior; the subsequent consolidation to dense glass with the characteristic stiffness and optical clarity of fused silica; and finally, optional further strengthening towards the theoretical limit at high temperatures. The correlative analysis approach demonstrated herein is expected to translate across feedstock resist systems and process routes, providing important groundwork for advancing rational thermal conversion protocols for the fabrication of high-fidelity precision structures and towards further expanding the accessible material bandwidth. Additionally, we show that the thermolysis of the POSS material unlocks a broad spectrum of accessible intermediate material states at low process temperatures, and demonstrates the fully converted silica to achieve a record tensile strength of 6 GPa.

Results and discussion

Thermal Analyses

To expand the general understanding of the POSS material's glass conversion, we established a correlative thermolysis approach combining in-situ micro-optical image tracking with simultaneous thermogravimetric analysis and differential scanning calorimetry (TGA/DSC) (Fig. 1). Figure 1A shows the composition of the used POSS-glass resist. Disk specimens with nominal diameters of 100 µm and heights of 25 µm were 2PP-printed, and their thermolysis conversion behavior inside an in-situ heating cell was observed via optical microscopy (Fig. 1B). TGA/DSC samples were drop-cast and cured via flood exposure. Together, the two measurements revealed the dimensional and visual evolution across the glass conversion and identified their interdependency with the underlying transformation reaction kinetics given by the mass loss and the heat flow data.

Figure 1C shows the POSS material's color evolution as observed during in-situ micro-optical thermolysis, along with the digital-image-correlation-measured (DIC) linear size corresponding to the specimen diameter. The color map corresponds to the average radial color distribution across the specimen surface as a function of temperature. In the temperature window between approximately 300 and 600 °C, the material is seen to undergo pronounced chromatic transitions. Along with emerging yellow and red discoloration, the material underwent continuous darkening, with a peak rate at 360 °C, until reaching the darkest point at around 425 °C. At higher temperatures, the material transitioned back to optical clarity in reverse order, where peak rates in lightening, red color loss, and yellow color

loss were observed successively at 520 °C, 540 °C, and 570 °C, with the latter shortly before reaching full transparency. Extended color analyses are provided in Supplementary Material S3. Dimensional measurements initially showed slight expansion of 1-2%, while the color remained unchanged. Coinciding with gradual yellowing close to 300 °C, major contraction set in with a pronounced size derivative peak near 350 °C. Until 440 °C the specimen size dropped to approximately 70% of its original dimension, as the color had progressively darkened to brown. After 440 °C, contraction slowed down notably with a minor derivative peak extending to about 520 °C, above which the relative size gradually approached a value near 60%, as the material regained full optical clarity.

TGA/DSC showed that the in-situ micro-optical observations were closely related to the glass conversion's key reaction stages, as identified by the major mass derivative and heat flow peaks (Fig. 1D, E). Above 300 °C, the initial decomposition stage with pronounced mass loss and exothermic heat flow is indicative of the thermo-oxidative disintegration of the cross-linked organic network and the volatilization of produced species[2,25,26]. Peaking between 350 °C and 400 °C, the TGA/DSC data well aligned with the equally pronounced dimensional contraction peak. This shows that volatilizations during the material conversion are directly mirrored by microstructural reorganizations that continuously condense the residual material. The simultaneously occurring chromatic transitions reveal further insights into the nature of the evolving intermediate material. The initial decomposition stage was accompanied by a continuous discoloration and concluded at around 440 °C, close to the darkest amber specimen color. Hence, the reaction stage produces light-absorbing and chromophoric species that accumulate within the material. The observed darkening indicates the formation of broadband-absorbing carbonaceous reaction products[2]. Yellow and red coloration may be attributed to oxygenated carbon species[27] and domains of sp^2-bonded graphitic clusters within amorphous carbon[27–29], both of which are increasingly absorbing towards the blue range of the visible light spectrum. The subsequent reaction stage at higher temperatures, centered around the smaller mass derivative and heat flow peaks near 520 °C, has been associated with the burn-off of such carbonaceous impurities to produce the final silica glass[2]. This is well supported by the simultaneously observed chromatic transformation back to a transparent colorless material. Consistent with the regained optical clarity, no notable changes in mass or heat flow are observed above approximately 600 °C. Indicating complete conversion of the inorganic POSS cages into silica glass, the TGA-measured final residual mass of ~32% closely matched the theoretically expected SiO_2 yield of 33% (Supplementary Material S2).

Mechanical Analyses

The material's mechanical transformation from the as-printed hybrid organic-inorganic POSS-acrylate to the final silica glass was characterized in both compression and tension, providing a comprehensive measure able to capture compression-tension asymmetries as typical of both polymers and brittle glass-ceramics. Based on the above thermal analyses, experiments were performed on specimens which were thermolyzed to selected target temperatures (Fig. 1F). Six different stages, including the as-printed hybrid polymer, intermediate states after 300 °C, 440 °C, and 520 °C, as well as the final glass state after 700 °C and 1000 °C, were selected. Uniaxial compression tests were conducted on cylindrical micropillars with nominal as-printed diameters of 15 µm and 20 µm, and a height-to-diameter aspect ratio of two. For the tensile experiments, we adapted our previously reported push-to-pull (P2P) approach[30,31], providing a swift characterization that circumvents the challenges around gripping microscale specimens. Therein, a mechanical conversion mechanism converts an applied compressive load to pull an integrated tensile specimen with a nominal as-printed gauge cross-section of 3 µm × 20 µm (Fig. 2A, Supplementary Material S4).

Our micro-mechanical characterizations revealed two distinct regimes of behavior across the material's polymer-to-glass transition. Figure 2B–E show representative stress-strain curves and SEM still frames captured at failure for both tension and compression.

From the as-printed state up to a treatment at 300 °C, the material behavior was characteristic of a rubber-like polymer, with soft initial responses followed by elongated stress plateaus. Both tension and compression of as-printed specimens showed minimal initial linear-elasticity below ~4% strain (insets Fig. 2B, C), with Young's moduli (E) of 0.5–0.6 GPa and yield stresses (σ_y) of 9-23 MPa. The average ultimate tensile strength (σ_{UTS}) was 129 MPa. While maintaining the same general behavior, treatment at 300 °C markedly increased all three properties by a factor of four to six, with E of 2.8-3.3 GPa, σ_y of 91–104 MPa, and σ_{UTS} = 465 MPa. The ultimate tensile strain (ε_{UTS}) at rupture decreased from typically above 60% in the as-printed state to below 40% after treatment at 300 °C (Fig. 2B). In compression, both as-printed and 300 °C-treated specimens failed near 50% strain under extended bulging followed by radial cracking (Fig. 2E), coinciding with an apparent steep stress increase.

Treatments above 300 °C showed a pronounced shift of the mechanical behavior to a ceramic-type, predominantly linear-elastic brittle response, as expected for the final glass products (Fig. 2B-F). Relative to 300 °C, treatment at 440 °C brought the strength into the GPa-range and increased the stiffness to >10 GPa, both well beyond the typical limits of polymeric materials. Simultaneously, ε_{UTS} sharply dropped to about 9%, as notable plasticity disappeared and failure switched to sudden brittle fracture. Likewise, in compression, no more bulging was observed with specimens failing by brittle crushing near 17% strain with observable vertical cracking (Fig. 2E). For treatments above 440 °C, the same qualitative behavior persisted, while strength and stiffness continued to increase towards the full conversion to glass.

The final silica glass treated at 700 °C exhibited ultra-high σ_{UTS} of 4.17 ± 0.46 GPa, which further treatment at 1000 °C increased to even higher values of 5.94 ± 0.45 GPa. Granted by substantial size-dependent strengthening[30,32], those values are subject to low scatter, exceed the strongest commercial glass fibers[33], and are roughly three times as strong as the well-studied pyrolytic carbon[1,34–36], whose σ_{UTS}, unlike that of our glass, is substantially reduced with respect to its compressive strength. Our tensile tests measured Young's moduli of 63.83 ± 2.29 GPa after 700 °C and 76.59 ± 2.67 GPa after 1000 °C. Both values are near our recent measurements of 71 ± 4 GPa[14] after treatment at 700 °C, which was obtained via precision marker-tracking-compression of micropillars. While modulus measurements from P2P tensile experiments are subject to some uncertainty, the herein obtained E values correspond to the common range of dense fused silica[37–40], in agreement with our previous TEM characterizations, which confirmed the material as amorphous silica with a homogeneous microstructure free from detectable pores and impurities[2].

The quantitative evolution of the measured mechanical properties across the polymer-to-glass conversion suggests a gradual transition of the dominant load-bearer from the initial organic network towards the emerging glass ceramic. Figure 2F–H show the progression of ε_{UTS}, E, and σ_{UTS}, respectively, all of which are well described by hyperbolic tangent fit functions (Supplementary Material S4), as reported for the property evolutions during similar polymer-to-ceramic conversions[41]. All conducted individual measurements are displayed; average values, standard deviations and the corresponding specimen numbers are provided in Supplementary Tables S1 and S2.

Analysis of the property evolution functions indicates three fundamental mechanical mechanisms underlying the glass conversion. Computing the temperature derivatives of the fitted trends estimates the rates at which each property changes, providing insight into the sequence of the governing mechanical transitions. The colored curves in Fig. 2F–H show the derivatives of the fits to ε_{UTS}, E, and σ_{UTS} form a cascade of three peaks, with the full width at half maximum (FWHM) each providing an approximation of the characteristic temperature interval of the major property transition. Mechanically, the glass conversion commences with a fairly rapid drop in deformability. In the model-estimated range of 250–350 °C, ε_{UTS} decreased well ahead of any similarly pronounced changes in E and σ_{UTS} and remained largely unchanged with the further heat treatment. The ε_{UTS} drop was aligned with the beginning major

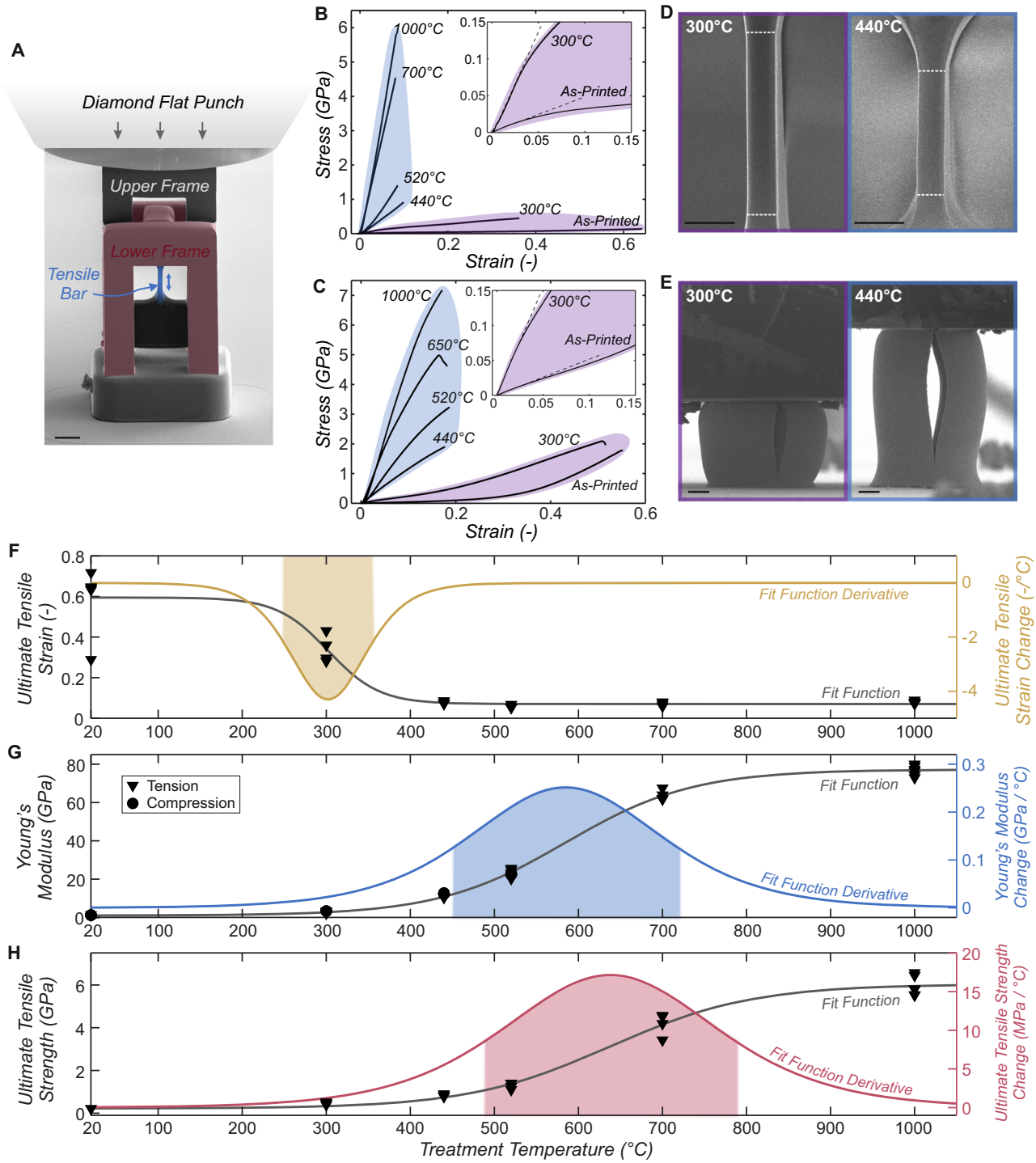


Fig. 2 | Mechanical property evolution of 2PP-printed POSS across the glass conversion process, as measured via uniaxial tension and compression of specimens heat treated at different temperatures. A colorized SEM image of a silica glass push-to-pull (P2P) tensile testing structure. Scale bar 10 µm; **B**, **C** Tensile and compressive stress-strain curves of specimens treated at the indicated increasing temperatures. Rubbery and glass-ceramic-type behaviors are highlighted in violet and blue, respectively. The 650 °C and 1000 °C compression curves in **C** are reproduced from our previous work[2]; **D**, **E** SEM still frames at failure of specimens thermolyzed at 300 °C and 440 °C. Scale bars: 3 µm; **F**–**H** Evolution of measured ultimate tensile strain, Young's modulus and tensile strength as a function of the thermolysis temperature. Each symbol corresponds to a single measurement.

dimensional contraction and the accompanying color transformation at the onset of the initial decomposition reaction stage (Fig. 1, Figure S2). The behavior is consistent with the beginning fragmentation of the long-range organic connectivity that eventually requires the loss of the viscoelastic chain extensibility, and which may be expected to be a prerequisite to the subsequent volatilization and accelerated mass loss. Interestingly, the chromatic transitions (Supplementary Material S3), show peak discoloration and darkening rates between 300 and 360 °C, providing a visual indicator, which may correlate with the advancing fragmentation of the organic network. Simultaneous with this process, increases in E and σ_{UTS} are seen to slowly blend in, suggesting the decomposition of the material's initial organic load bearer is mechanically outweighed by the formation of a

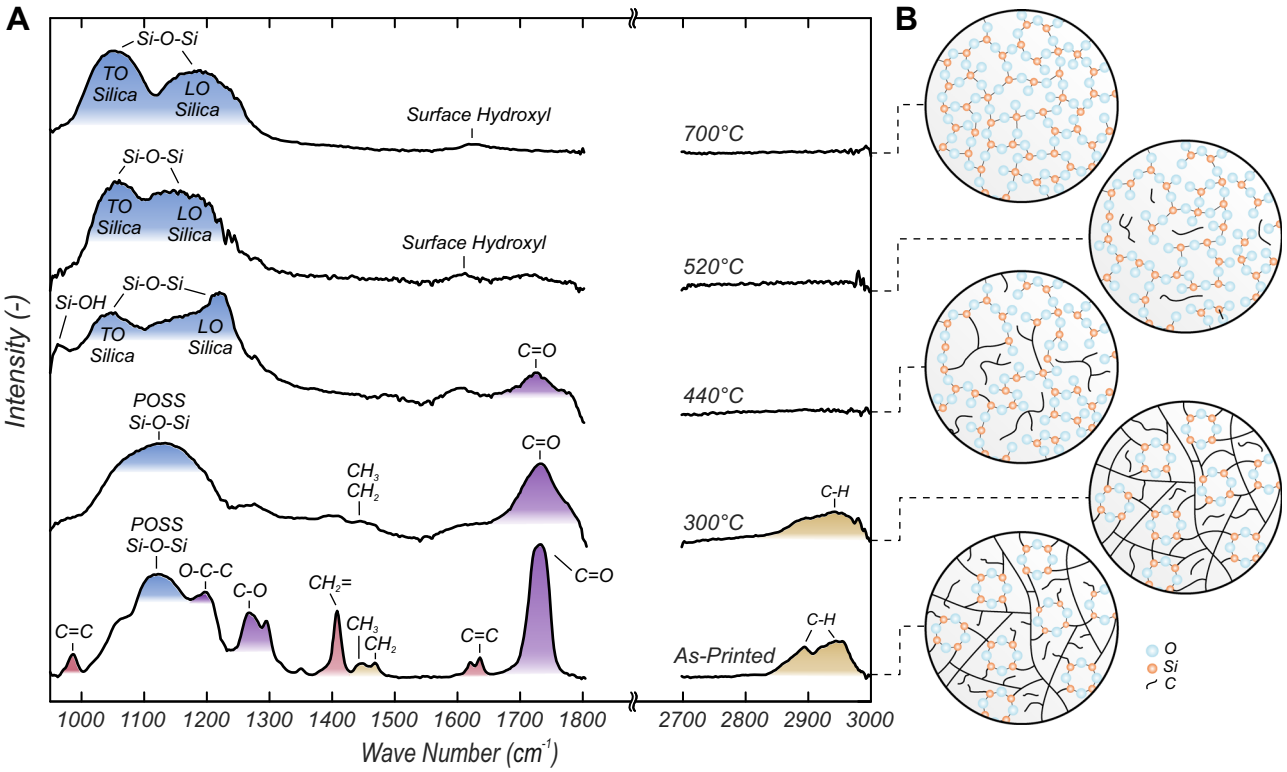


Fig. 3 | Chemical evolution of 2PP-printed POSS across the glass conversion process. A Optical photothermal infrared (O-PTIR) spectra after thermolysis at the indicated temperatures; inorganic signatures are color coded in blue, signals associated with organic features are marked in purple (acrylate ester groups), red (uncrosslinking acrylic groups) and yellow (organic chain-backbones) **B** Schematic microstructure evolution visualizing the transformation from the initial crosslinked organic–inorganic hybrid network to the final fused silica glass.

new interconnected phase – the silica glass network. The model-estimated major Young's modulus increase between 450 and 720 °C indicates this newly forming glass network to then gradually consolidate, consistent with the observed reactions removing residual decomposition fragments in the same temperature range. Providing another useful visual proxy, the most rapid reduction in chromaticity back to a transparent material (Supplementary Material S3) aligns with the most pronounced mechanical stiffening. This suggests that full condensation of the silica network is driven by the removal of residual carbonaceous impurities, and indicates that these act as softening free species rather than stiffening substitution impurities[42,43]. Concurrent strengthening of the material is found to extend to higher temperatures. Our model-estimate suggests the primary strengthening window within 490–790 °C, in agreement with previously found strength gains when the treatment temperature was increased from 650 °C to 1000 °C[2]. Such continuing strengthening is consistent with the microstructural reorganization of residual ring-like Si-O structures – a potential relic from the POSS cages - to tetrahedral units, which we had reported in our previous study[2].

Chemical Analyses

Complementing the identified micro-optical and -mechanical transformations, we present optical photothermal infrared (O-PTIR) spectroscopy[44] measurements which revealed the POSS material's corresponding chemical evolution (Fig. 3). While the POSS-acrylate possesses a characteristic IR-signature[45], the small size of 2PP-printed specimens severely limits characterization by conventional infrared techniques. Micro-Raman spectroscopy, on the other hand, is hindered by the strong luminescence[46] of defective silicon-oxygen networks, such as present in the intermediate polymer–glass states. Overcoming both challenges, O-PTIR employs indirect photothermal excitation with a visible-light probe, yielding highly resolved chemical information. Measurements were performed on 2PP-printed micropillars subjected to the same thermolysis treatments as the mechanical specimens. The spectral range of the measurement hardware included 900-1800 cm^{-1} and 2700-3000 cm^{-1}.

Figure 3 shows the measured spectra after thermal treatments at progressively increasing temperatures along with schematic representations of the corresponding microstructure evolution. Inorganic spectral signatures are highlighted in blue, while different organic signals are marked in purple, red and yellow.

In the as-printed state, the POSS material consists of a crosslinked polymer network, formed by free-radical polymerization of the acrylic groups of both the POSS monomer and the trifunctional acrylate (Fig. 1A), within which the inorganic silicon-oxygen POSS cages are embedded. The O-PTIR spectrum clearly reflects this chemically heterogeneous organic-inorganic structure. In the fingerprint region, the dominant band at 1123 cm^{-1} is characteristic of the silicon-oxygen POSS cages[45,47–49] and corresponds to the asymmetric stretching of the Si-O-Si bridges in the closed rings forming the faces of the POSS cages. The shoulder near 1056 cm^{-1} can be attributed to the symmetric ring mode, which expectedly is comparably weak due to the symmetry of the siloxane cages[47]. The rest of the spectrum reflects different features of the organic network. The dominating peaks at 1732 cm^{-1}, 1268 cm^{-1} and 1197 cm^{-1}, respectively, correspond to the stretching of C = O[50–53], C-O[50] and C-C-O[53–55] bonds of ester groups. This strong ester signature originates from the acrylic groups present in all functional branches of both the POSS monomer and the triacrylate crosslinker. Characteristic C-H stretching of methylene groups[56–58] in the chain backbones is observed in the region at 2850-3000 cm^{-1}, along with corresponding C-H bending modes at 1468 cm^{-1} and 1447 cm^{-1}. Furthermore, residual uncrosslinked acrylic groups are evident from the C = C stretching[53,59] and C = C twisting[56] modes at 1635 cm^{-1} and 986 cm^{-1}, respectively, as well as from $=CH_2$ scissoring[56] at 1408 cm^{-1}.

From the as-printed state to 300 °C, the material's general chemical structure remained largely intact as the organic constituents underwent notable disordering and onsetting fragmentation. While the apparent peak

broadening suggests emerging disorder, the persistence of the 1131 cm^{-1} Si-O-Si band, as well as the C-H stretching bands at 2850–3000 cm^{-1} indicate that both the inorganic POSS cages and the hydrocarbon backbones of the organic network remained largely preserved. Most other organic signatures more markedly decreased in intensity, with several signals nearly vanishing. Generally, this is indicative of the onsetting decomposition, which would be expected to decrease mechanical properties. However, weakening of the C = C bond-related peaks is characteristic of thermal post-curing[60,61], which can significantly enhance the mechanical properties of 2PP-printed acrylates. The found strength and stiffness increase upon treatment at 300 °C indicate that thermally induced cross-linking outweighed the onsetting degradation at this stage.

The spectrum collected after treatment at 440 °C revealed a distinct microstructural transition, consistent with the found pronounced mechanical shift from polymeric to glass-ceramic behavior. The complete disappearance of C-H stretching vibrations indicates that the backbone chains of the organic network had disintegrated. Only minor organic fragments appear to persist, as evidenced by the further weakened and diffuse residual C = O absorption. Simultaneously, the signatures associated with the silicon-oxygen POSS cages had disappeared, while two distinct bands near 1220 cm^{-1} and 1048 cm^{-1} formed, which are characteristic of tetrahedral amorphous silica glass, where they correspond to the longitudinal-optical (LO) and the transverse-optical (TO) components of the asymmetric Si-O-Si stretching mode[62,63], respectively. The concurrent appearance of a silanol stretching vibration[64] at 967 cm^{-1} indicates the presence of partially condensed silica pre-stages. Hence, the spectral data indicates the cleavage of the discrete POSS cages and the reorganization of the silicon-oxygen-species to a silica glass network. In combination with the observed shift to a glass-ceramic-type mechanical behavior one may conclude that the primary load-bearer had by 440 °C largely translated from the initial organic network to the newly forming silica glass.

Upon heating to 520 °C, the silica network became more defined as the organic signatures vanished. Mirroring the mechanical behavior, the largely disappeared silanol band indicates that condensation reactions forming bridging Si-O-Si bonds were well advanced, with the LO and TO stretching bands approaching the final fused silica glass signature. Simultaneously, trace contributions from carbonyl-containing species remained the only measured signal which may be associated with organic fragments. Yet, our previous micro-Raman measurements had identified significant residual carbonaceous species at this thermolysis stage[2], consistent with the herein observed remaining yellow color and the TGA/DSC tails (Fig. 1, Supplementary Material S3). Inorganic carbon chars have an indistinct IR response[65,66] but produce pronounced Raman scattering[67,68]. Together, the O-PTIR and the micro-Raman data suggest that the residual light-absorbing species may be largely traced back to such.

After treatment at 700 °C, the spectrum exhibited the fully developed LO and TO components of the asymmetric Si–O–Si stretching characteristic of fused silica[62,63]. Consistent with the restored optical clarity and the measured Young's modulus, this renders the material as dense silica glass, as confirmed by our previous TEM measurements[2]. The weak feature near 1605 cm^{-1} is attributed to surface hydroxyl groups[69] from ambient humidity.

Conclusion

Collectively, the presented thermal, mechanical, and spectroscopic analyses revealed a comprehensive picture of the mechanisms governing the polymer-to-glass conversion of the POSS material system on the microscale. We found that the thermolysis proceeds through a series of consecutive intermediate steps within distinct model-estimated temperature windows. In the early phase up to ~300 °C, onsetting decomposition and thermally induced cross-linking of the organics are competing. While first decomposition products initiate discoloration and dimensional contraction sets in, the material retains its initial rubber-elastic mechanical behavior, albeit with significantly enhanced stiffness and strength. Temperatures exceeding 300 °C then rapidly accelerate the decomposition with pronounced mass loss, dimensional contraction and chromatic darkening. As the organic matrix disintegrates, the dispersed inorganic POSS cages undergo cleavage and condense into a silica network at temperatures more than 500 °C below the melting point of SiO_2. Concurrently, a pronounced shift in mechanical behavior indicates the transitions of the primary load-bearer from the decomposing rubber-elastic organic matrix to the newly forming glass ceramic phase. Above 440 °C, the thermolysis then gradually oxidizes and removes residual carbonaceous byproducts from the organic decomposition, which allows the material to consolidate to pure fused silica, regaining optical clarity and achieving the characteristic mechanical properties of dense glass. Treatment above 700 °C further strengthens the material towards its theoretical limit, consistent with continued reorganization of the short-range silica network toward a more tetrahedral structure[2].

The insights obtained pave the way for POSS-glass conversion protocols refined for minimal processing time at the highest reproducibility. They further highlight the potential of partial thermolysis treatments to access a wide range of intermediate properties, including more than two orders of magnitude in mechanical stiffness and strength, spanning from rubbery-soft to ultra-strong and stiff. Treatment temperatures as low as 440 °C already yield ceramic-type behavior with gigapascal-range strength. Substantial optical clarity is recovered above ~575 °C, opening opportunities for microsystems applications involving more temperature-sensitive components, such as conductive aluminum metallization layers. Further, the fully converted POSS-glass is uniquely suited for the most demanding micromechanical applications, setting the benchmark for tensile strength among 2PP-derived materials at 6 GPa.

More broadly, our findings establish a fundamental understanding of thermal conversion routes in 2PP-printing, expected to translate to other feedstock resist systems and to provide important groundwork to advance existing routes and to further expand the technique towards currently unavailable technologically relevant materials. In particular, our work identifies the early formation of a mechanically self-supporting inorganic continuum prior to the disintegration of the initially load-bearing organic framework as crucial for the successful fabrication of high-fidelity precision structures. Rational thermolysis temperature-time protocols offer key control leverage towards this end and can be optimized via the correlative analysis approach established herein.

Materials and methods

Preparation of POSS-Glass Resist

Adopting our previously introduced formulation[2], the prepared POSS-glass resist consisted of three parts (Fig. 1A): (i) 89 wt% of acryloxypropyl POSS cage mixture (MA0736, Hybrid Plastics) with the general formula $(RSiO_{1.5})_n$ with $R = C_6H_9O_2$ and $n = 8, 10, 12$, which is comprised of inorganic silsesquioxane cages, to which cross-linkable acrylic groups attach at the Si-atom-corners; (ii) 8.6 wt% of ethoxylated (6) trimethylolpropane triacrylate (SR499, Sartomer), a highly-flexible trifunctional acrylic monomer; and (iii) 2.4 wt% of the Norrish Type I photoinitiator 2-benzyl-2-dimethylamino−1-(4-morpholinophenyl)-butanone−1 (Irgacure 369, CIBA Specialty Chemicals). Under UV-protected environment, the acryloxypropyl POSS was first mixed with the Irgacure 369 photoinitiator in a glass vial, followed by adding the trifunctional acrylate. The mixture was then magnetically stirred at 75 °C for 12 h using an oil bath. After the photoinitiator was fully dissolved, the final homogeneous and transparent resist was obtained. After cooling to room temperature, the resist was ready to use and stored under ambient UV-protected conditions.

Specimen Fabrication

Specimens for in-situ micro-optical thermolysis, mechanical testing, and O-PTIR spectroscopy were 2PP printed from the POSS-glass resist using a commercial Photonic Professional GT2 2PP system (Nanoscribe), equipped with a 50 mW, 780 nm FemtoFiber pro NIR pulsed laser (TOPTICA Photonics), and a Plan-Apochromat 63x/NA1.4 Oil DIC M27 objective lens (Carl Zeiss). The objective lens was directly immersed into the resist, which was drop-cast on 25 × 25 × 0.7 mm silicon substrates for the printing of mechanical and O-PTIR spectroscopy structures, and on circular glass

substrates with a diameter of 7 mm and a thickness of 300 µm to manufacture the in-situ micro-optical thermolysis specimens. After printing, samples were immersed in isopropanol for 20 min and subsequently for 5 min in PGMEA to remove uncured resist, followed by supercritical drying in a critical point dryer EM CPD300 (Leica Microsystems). TGA/DSC samples were drop-cast and cured via 20-min-long linear flood exposure with a UV-EXP 150S UV lamp (Idonus) with a peak wavelength of 405 nm and an average light intensity of 40 mW/cm^2.

Specimens for mechanical testing and O-PTIR spectroscopy were heat treated using a TS1 12/60/600 split tube furnace (Carbolite Gero) in ambient air (Figure S1). Five different target temperatures of 300 °C, 440 °C, 520 °C, 700 °C, and 1000 °C, respectively, were investigated in addition to untreated, as-printed samples. All thermal treatments comprised an initial ramp to 275 °C at 3 °C/min, before heating to the target temperatures at a rate of 1 °C/min. After a 60 min hold, the samples were cooled down to room temperature.

Experimental Characterizations

in-situ micro-optical thermolysis was conducted with a TS1500 heating cell (Linkam Scientific Instruments), and observed with a DSX1000 digital microscope (Olympus Corporation) using a 10x objective lens. Specimens were heated with the same temperature profile as the mechanical samples with the target temperature of 700 °C (Figure S1). The linear specimen size was determined as the DIC-measured diameter relative to the initial as-printed value, and the color evolution was extracted from the top surface as the RGB-values along 15 concentric rings with different diameters, each comprised of 24 equidistant points. To condense the spatial color data to the mean radial distribution, the RGB-values were averaged over each ring. TGA and DSC were simultaneously measured using a Sensys Evo thermal analyzer (Setaram) in air atmosphere with a flow rate of 20 sccm, applying a constant heating rate of 1 °C/min.

in-situ SEM micro-mechanical experiments were conducted using a Hysitron PI 89 Picoindenter (Bruker) and an Alemnis Standard Assembly (Alemnis) nanoindenter inside a Gemini 2 and an Auriga (Carl Zeiss) SEM, respectively. All samples were glued on short-pin SEM stubs, and sputter-coated with a conductive silver layer of ~12 nm thickness. Engineering stress-strain curves were calculated from the recorded load-displacement data using SEM-measured specimen dimensions (Supplementary Material S4). The strain data were compliance-corrected by DIC tracking of the recorded SEM footage. Young's moduli (E) were determined from the maximum slope of the initial linear-elastic region of the stress-strain curves. The measured yield strengths (σ_y) correspond to the 0.2% offset yield stresses. Ultimate tensile strengths (σ_{UTS}) and ultimate tensile strains (ε_{UTS}) were determined as the maximum values prior to rupture.

O-PTIR measurements were carried out with a mIRage-LS sub-micron IR multimodal microscope (Photothermal Spectroscopy Corp.). Spectra were collected from micropillars with nominal as-printed heights and diameters of 30 µm.

Data availability

All data related to this work is published in the open-access data repository of the Karlsruhe Institute of Technology (KIT) [https://doi.org/10.35097/jd0rqhd5rzqyx0n2].

Received: 23 June 2026; Accepted: 9 October 2026;
Published online: 30 October 2026

References

1. Bauer, J., Schroer, A., Schwaiger, R. & Kraft, O. Approaching theoretical strength in glassy carbon nanolattices. *Nat. Mater.* **15**, 438–443 (2016).
2. Bauer, J., Crook, C. & Baldacchini, T. A sinterless, low-temperature route to 3D print nanoscale optical-grade glass. *Science* **380**, 960–966 (2023).
3. Gonzalez-Hernandez, D. et al. Laser 3D Printing of Inorganic Free-Form Micro-Optics. *Photonics* **8**, 577 (2021).
4. Huang, P. H. et al. Three-dimensional printing of silica glass with sub-micrometer resolution. *Nat. Commun.* **14**, 3305 (2023).
5. Ye, P., Hong, Z., Loy, D. A. & Liang, R. Solvent-Free Silsesquioxane Self-Welding for 3D Printing Multi-Refractive Index Glass Objects. *Adv. Optical Mater.* **12**, 2400783 (2024).
6. Brigo, L. et al. 3D Nanofabrication of SiOC Ceramic Structures. *Adv. Sci.* **5**, 1800937 (2018).
7. Bauer, J. et al. Additive Manufacturing of Ductile, Ultrastrong Polymer-Derived Nanoceramics. *Matter* **1**, 1547–1556 (2019).
8. Vyatskikh, A., Ng, R. C., Edwards, B., Briggs, R. M. & Greer, J. R. Additive Manufacturing of High-Refractive-Index, Nanoarchitected Titanium Dioxide for 3D Dielectric Photonic Crystals. *Nano Lett.* **20**, 3513–3520 (2020).
9. Liu, J. et al. 3D Printing Nano-Architected Semiconductors Based on Versatile and Customizable Metal-Bound Composite Photoresins. *Adv. Mater. Technol.* **7**, 2101230 (2022).
10. Jiang, M. et al. Lightweight and ultrastrong 3D nanoarchitected high-entropy ceramic metamaterials. *Sci. Adv.* **11**, eadw6632 (2025).
11. Vyatskikh, A. et al. Additive manufacturing of 3D nano-architected metals. *Nat. Commun.* **9**, 593 (2018).
12. Luitz, M. et al. High Resolution Patterning of an Organic–Inorganic Photoresin for the Fabrication of Platinum Microstructures. *Adv. Mater.* **33**, 2101992 (2021).
13. Wen, X. et al. 3D-printed silica with nanoscale resolution. *Nat. Mater.* **20**, 1506–1511 (2021).
14. Schneider, J. L. G., Liang, J., Somers, P., Wegener, M. & Bauer, J. Two-Photon Grayscale Lithography (2GL) of High Mechanical and Optical Quality 3D Silica Glass Microstructures. *Adv. Funct. Mater.* **36**, https://doi.org/10.1002/adfm.77318 (2026).
15. Baldacchini, T. *Three-Dimensional Microfabrication Using Two-Photon Polymerization*. (Elsevier, Amsterdam, 2019).
16. Institute of Applied Physics, Karlsruhe Institute of Technology. 3D Printing Speed: Compare Speed and Minimum Feature Size. Karlsruhe Institute of Technology (KIT) https://3dprintingspeed.aph.kit.edu/.
17. Bauer, J. et al. Nanolattices: An Emerging Class of Mechanical Metamaterials. *Adv. Mater.* **29**, 1701850 (2017).
18. Cheng, W. et al. Unlocking superior fracture resistance in micro-ceramics for architected meta-materials via ALD stress engineering. *Acta Materialia* **301**, 121474 (2025).
19. Wang, H. et al. Two-Photon Polymerization Lithography for Optics and Photonics: Fundamentals, Materials, Technologies, and Applications. *Adv. Funct. Mater.* **33**, 2214211 (2023).
20. Faraji Rad, Z., Prewett, P. D. & Davies, G. J. High-resolution two-photon polymerization: the most versatile technique for the fabrication of microneedle arrays. *Microsyst. Nanoengineering* **7**, 71 (2021).
21. Zhang, W. et al. Nanoscale 3D printing of glass photonic crystals with near-unity reflectance in the visible spectrum. *Sci. Adv.* **11**, eadv0267 (2025).
22. Hong, Z., Ye, P., Loy, D. A. & Liang, R. Integrated 3D Printing of Transparency-on-Demand Glass Microstructure. *Adv. Optical Mater.* **13**, 2500390 (2025).
23. Schwab, J. J. & Lichtenhan, J. D. Polyhedral Oligomeric Silsesquioxane (POSS)-Based Polymers. *Appl. Organomet. Chem.* **12**, 707–713 (1998).
24. Kotz, F. et al. Two-Photon Polymerization of Nanocomposites for the Fabrication of Transparent Fused Silica Glass Microstructures. *Adv. Mater.* **33**, 2006341 (2021).
25. Goswami, A., Srivastava, G., Umarji, A. M. & Madras, G. Thermal degradation kinetics of poly(trimethylol propane triacrylate)/poly(hexane diol diacrylate) interpenetrating polymer network. *Thermochim. Acta* **547**, 53–61 (2012).

26. Li, L., Liang, R., Li, Y., Liu, H. & Feng, S. Hybrid thiol–ene network nanocomposites based on multi(meth)acrylate POSS. *J. Colloid Interface Sci.* **406**, 30–36 (2013).
27. Sun, H., Biedermann, L. & Bond, T. C. Color of brown carbon: A model for ultraviolet and visible light absorption by organic carbon aerosol. *Geophys. Res. Lett.* **34**, L17813 (2007).
28. Bond, T. C. & Bergstrom, R. W. Light Absorption by Carbonaceous Particles: An Investigative Review. *Aerosol Sci. Technol.* **40**, 27–67 (2006).
29. Bond, T. C. Spectral dependence of visible light absorption by carbonaceous particles emitted from coal combustion. *Geophys. Res. Lett.* **28**, 4075–4078 (2001).
30. Bauer, J. et al. Push-to-pull tensile testing of ultra-strong nanoscale ceramic–polymer composites made by additive manufacturing. *Extrem. Mech. Lett.* **3**, 105–112 (2015).
31. Bauer, J., Schroer, A., Schwaiger, R. & Kraft, O. The Impact of Size and Loading Direction on the Strength of Architected Lattice Materials. *Adv. Eng. Mater.* **18**, 1537–1543 (2016).
32. Brambilla, G. & Payne, D. N. The ultimate strength of glass silica nanowires. *Nano Lett.* **9**, 831–835 (2009).
33. Wallenberger, F. T. Commercial and experimental glass fibers. in *Fiberglass and Glass Technology: Energy-Friendly Compositions and Applications* 3–90 (Springer US, 2010). https://doi.org/10.1007/978-1-4419-0736-3_1.
34. Albiez, A. & Schwaiger, R. Size Effect on the Strength and Deformation Behavior of Glassy Carbon Nanopillars. *MRS Adv.* **4**, 133–138 (2019).
35. Rossi, E., Bauer, J. & Sebastiani, M. Humidity-Dependent Flaw Sensitivity in the Crack Propagation Resistance of 3D-Printed Nano-Ceramics. *Scr. Materialia* **194**, 113684 (2021).
36. Zhang, X. et al. Theoretical strength and rubber-like behaviour in micro-sized pyrolytic carbon. *Nat. Nanotechnol.* **14**, 762–769 (2019).
37. Sinani, T. et al. A novel Peltier based low temperature in situ nanoindentation system. *Rev. Sci. Instrum.* **96**, 115204 (2025).
38. Adachi, T. & Sakka, S. Dependence of the elastic moduli of porous silica gel prepared by the sol-gel method on heat-treatment. *J. Mater. Sci.* **25**, 4732–4737 (1990).
39. Zhang, L., Gain, A. K. & Li, Z. Exploring the deformation mechanisms and mechanical properties of fused silica through nanoindentation and ramp-nanoscratching. *Wear* **571**, 205812 (2025).
40. Brückner, R. Properties and structure of vitreous silica. I. *J. Non-Crystalline Solids* **5**, 123–175 (1970).
41. Larson, N. M. & Zok, F. W. In-situ 3D visualization of composite microstructure during polymer-to-ceramic conversion. *Acta Materialia* **144**, 579–589 (2018).
42. Sorarù, G. D., Kundanati, L., Santhosh, B. & Pugno, N. Influence of free carbon on the Young's modulus and hardness of polymer-derived silicon oxycarbide glasses. *J. Am. Ceram. Soc.* **102**, 907–913 (2019).
43. Sorarù, G. D., Dallapiccola, E. & D'Andrea, G. Mechanical Characterization of Sol–Gel-Derived Silicon Oxycarbide Glasses. *J. Am. Ceram. Soc.* **79**, 2074–2080 (1996).
44. Olson, N. E., Xiao, Y., Lei, Z. & Ault, A. P. Simultaneous Optical Photothermal Infrared (O-PTIR) and Raman Spectroscopy of Submicrometer Atmospheric Particles. *Anal. Chem.* **92**, 9932–9939 (2020).
45. Choi, J. H. et al. Preparation of polymer/POSS nanocomposites by radiation processing. *Radiat. Phys. Chem.* **78**, 517–520 (2009).
46. Salh, R. Defect Related Luminescence in Silicon Dioxide Network: A Review. in *Crystalline Silicon - Properties and Uses* (IntechOpen, 2011). https://doi.org/10.5772/22607.
47. Park, E. S., Ro, H. W., Nguyen, C. V., Jaffe, R. L. & Yoon, D. Y. Infrared spectroscopy study of microstructures of poly(silsesquioxane)s. *Chem. Mater.* **20**, 1548–1554 (2008).
48. Wang, B., Shi, M., Ding, J. & Huang, Z. Polyhedral oligomeric silsesquioxane (POSS)-modified phenolic resin: Synthesis and anti-oxidation properties. *E-Polym.* **21**, 316–326 (2021).
49. Zhao, H. et al. Polyurethane/POSS nanocomposites for superior hydrophobicity and high ductility. *Compos. Part B: Eng.* **177**, 107441 (2019).
50. O'Reilly, J. M. & Mosher, R. A. Conformational Energies of Stereoregular Poly(methyl methacrylate) by Fourier Transform Infrared Spectroscopy. *Macromolecules* **14**, 602–608 (1981).
51. Yao, S. F., Chen, X. T. & Ye, H. M. Investigation of Structure and Crystallization Behavior of Poly(butylene succinate) by Fourier Transform Infrared Spectroscopy. *J. Phys. Chem. B.* **121**, 9476–9485 (2017).
52. Wang, Z. et al. Study about the effect of cellulose nanocrystals on a polyacrylate miniemulsion. *RSC Adv.* **15**, 7181–7190 (2025).
53. Zhou, C., Wang, Q. & Wu, Q. UV-initiated crosslinking of electrospun poly(ethylene oxide) nanofibers with pentaerythritol triacrylate: Effect of irradiation time and incorporated cellulose nanocrystals. *Carbohydr. Polym.* **87**, 1779–1786 (2012).
54. Smith, B. C. Infrared Spectroscopy of Polymers X: Polyacrylates. *Spectroscopy* **38**, 10–14 (2023).
55. Smith, B. C. The C=O Bond, Part VI: Esters and the Rule of Three. *Spectroscopy* **33**, 20–23 (2018).
56. Carmona, P. & Moreno, J. The infrared spectra and structure of methyl acrylate. *J. Mol. Struct.* **82**, 177–185 (1982).
57. Feairheller, W. R. & Katon, J. E. The vibrational spectra of acrylic acid and sodium acrylate*. *Spectrochimica Acta* **23A**, 2225–2232 (1967).
58. Nagai, H. Infrared spectra of stereoregular polymethyl methacrylate. *J. Appl. Polym. Sci.* **7**, 1697–1714 (1963).
59. Orgill, M., Baker, B. L. & Owen, N. L. FTIR studies of conformational isomerism in acrylates and acrylic acids. *Spectrochimica Acta* **55**, 1021–1024 (1999).
60. Bauer, J., Izard, A. G., Zhang, Y., Baldacchini, T. & Valdevit, L. Thermal post-curing as an efficient strategy to eliminate process parameter sensitivity in the mechanical properties of two-photon polymerized materials. *Opt. Express* **28**, 20362 (2020).
61. Schroer, A., Bauer, J., Schwaiger, R. & Kraft, O. Optimizing the mechanical properties of polymer resists for strong and light-weight micro-truss structures. *Extrem. Mech. Lett.* **8**, 283–291 (2016).
62. Zhang, C. C. et al. ATR-FTIR spectroscopic studies on density changes of fused silica induced by localized CO2 laser treatment. *Chin. Phys. B.* **24**, 024220 (2015).
63. Almeida, R. M. Detection of LO modes in glass by infrared reflection spectroscopy at oblique incidence. *Phys. Rev. B.* **45**, 161–170 (1992).
64. Bertoluzza, A., Fagnano, C., Morelli, M. A., Gottardi, V. & Guglielmi, M. Raman and infrared spectra on silica gel evolving toward glass. *J. Non-Cryst. Solids* **48**, 117–128 (1982).
65. Russo, C., Stanzione, F., Tregrossi, A. & Ciajolo, A. Infrared spectroscopy of some carbon-based materials relevant in combustion: Qualitative and quantitative analysis of hydrogen. *Carbon* **74**, 127–138 (2014).
66. Russo, C. *et al*. Separation and characterization of size-segregated fractions (soot and char) of carbonaceous particulate produced from coal pyrolysis. In (XXXIX Meeting of the Italian Section of the Combustion Institute, 2016).
67. Ferrari, A. C. & Robertson, J. Interpretation of Raman spectra of disordered and amorphous carbon. *Phys. Rev. B.* **61**, 14095–14107 (2000).
68. Sadezky, A., Muckenhuber, H., Grothe, H., Niessner, R. & Pöschl, U. Raman microspectroscopy of soot and related carbonaceous materials: Spectral analysis and structural information. *Carbon* **43**, 1731–1742 (2005).
69. Davis, K. M. & Tomozawa, M. Water diffusion into silica glass: structural changes in silica glass and their effect on water solubility and diffusivity. *J. Non-Crystalline Solids* **185**, 203–220 (1995).

Acknowledgements

We thank Photothermal Spectroscopy Corp. for enabling the O-PTIR measurements.

Author contributions

J.L.: Investigation (lead), Formal Analysis (lead), Methodology (lead), Software (support), Validation (equal), Visualization (lead), writing – original draft (lead), writing - review & editing (equal). L.H.: Investigation (support), Formal Analysis (support), Methodology (equal), Software (lead), Validation (equal), Visualization (support), writing – original draft (support), writing - review & editing (equal). P.A.: Investigation (support), Methodology (equal), Validation (support), writing - review & editing (support). J.B.: Conceptualization, Funding Acquisition, Project Administration, Supervision, Investigation (support), Methodology (support), Validation (support), Writing – Original Draft (support), Writing -Review & Editing (equal).

Funding

We acknowledge funding by the Deutsche Forschungsgemeinschaft (DFG, German Research Foundation) under the grant BA 5778/2−1, as well as under Germany's Excellence Strategy for the Excellence Cluster "3D Matter Made to Order" (2082/1–390761711; 2082/2–390761711), by the Carl Zeiss Foundation, by the Helmholtz program Materials Systems Engineering and by the Karlsruhe Nano Micro Facility (KNMFi). Open Access funding enabled and organized by Projekt DEAL.

Competing interests

The authors declare no competing interests.

Additional information

Supplementary information The online version contains supplementary material available at https://doi.org/10.1038/s43246-026-01420-6.

Correspondence and requests for materials should be addressed to Jens Bauer.

Peer review information *Communications Materials* thanks the anonymous reviewers for their contribution to the peer review of this work.

Reprints and permissions information is available at http://www.nature.com/reprints

Publisher's note Springer Nature remains neutral with regard to jurisdictional claims in published maps and institutional affiliations.

Open Access This article is licensed under a Creative Commons Attribution 4.0 International License, which permits use, sharing, adaptation, distribution and reproduction in any medium or format, as long as you give appropriate credit to the original author(s) and the source, provide a link to the Creative Commons licence, and indicate if changes were made. The images or other third party material in this article are included in the article's Creative Commons licence, unless indicated otherwise in a credit line to the material. If material is not included in the article's Creative Commons licence and your intended use is not permitted by statutory regulation or exceeds the permitted use, you will need to obtain permission directly from the copyright holder. To view a copy of this licence, visit http://creativecommons.org/licenses/by/4.0/.

© The Author(s) 2026